Morphology of Evaporated Multiblock Copolymer Membranes Studied by Molecular Dynamics Simulations

Mesfin Tsige,* Thomas R. Mattsson, and Gary S. Grest

Sandia National Laboratories, Albuquerque, New Mexico 87185

Received July 20, 2004; Revised Manuscript Received September 9, 2004

ABSTRACT: We present extensive simulations modeling the casting of multiblock polymer films by evaporation. The domain structure of the resulting film is strongly affected by varying the relative stiffness of the coblocks. The morphology changes from a bicontinuous lamellar phase when both blocks are flexible to a small-scale phase-separated phase with isolated domains as the stiffness of one of the blocks increases. As the relative stiffness of the blocks changes, the rate of evaporation, interfacial width, and morphology of the system changes. The findings can be used to tailor membrane morphology of interest to fuel-cell applications where the morphology is important for proton conduction.

1. Introduction

Polymer thin films that contain well-defined patterns are of current interest, especially due to their potential application for nanotechnology,[1−10] such as nanowires, quantum dots, nanolithography to mention a few. Block copolymers are known to self-assemble into a periodic array, making them an ideal candidate for this application. Block copolymers consist of two or more homopolymer chains or blocks that are covalently bonded at their chain ends to form a single polymer chain. In bulk, the immiscibility and molecular connectivity between the block segments give rise to well-organized periodic domain microstructures. In general, the dimensions of the blocks and the segment−segment interaction parameters control the size and shape of these domains. Diblock copolymers are well studied and known to form ordered nanostructures such as lamellar, cylindrical, and spherical nanostructures by simply changing the molecular weight of the two components.[11,12]

In block copolymer thin films the microdomain structure is also controlled by interfacial interactions at the substrate and air surfaces.[12−20] Preferential attraction of one of the blocks by these surfaces forces the microdomain morphology to a surface-directed parallel orientation.[14,21−24] Perpendicular orientation of the microdomain has been observed when the surfaces become neutral or have no preference for either of the two blocks.[4,14,22,23,25,26] Under asymmetric boundary conditions, e.g., a neutral substrate but a nonneutral air surface, a mixed morphology of parallel near the air surface and perpendicular adjacent to the substrate has been observed. Perpendicular orientation of the microdomain morphology also can be achieved by applying external fields,[27,28] varying film thickness,[29] solvent casting,[30] and recently substrate roughness.[31]

The morphology of block copolymers also can be controlled by varying the stiffness of the different block segments and is the focus of the present study. One of the many applications of block copolymers is for fuel-cell membranes. Development of new materials continues to be the fundamental challenge in making fuel cells highly efficient. A fuel cell is a complex system where catalysis, ionic conduction, and transport in polymer membranes all combine to the overall efficiency. The polymer membrane separating the cathode and anode is in the heart of the device: it needs to be an electronic insulator as well as an ionic conductor. It also must separate fuel and products and of course must be mechanically stable. Since the catalysis is more efficient at high temperature, the thermal stability of the membrane is an important design parameter for the device. Traditional membranes includes Nafion.[32] However, in Nafion, proton conduction occurs in water through channels in the material, which limits the operating temperature. Alternative membranes include sulfonated polyetherketones.[33] Successful membrane materials combine hydrophobic and hydrophilic characters, for example, in backbone and side chains to create a microscopic phase separation, enhancing proton conduction. An alternative is to build a block copolymer $(AB)_n$ with alternating hydrophobic and hydrophilic segments.

Often high-performance polymer thin films are produced by evaporating the solvent from a polymer solution. The technique enables morphology of thin films that are outside the normal, equilibrium state, which in many cases is advantageous.[34,35] From a computational perspective, modeling block copolymer films is much more difficult than homopolymer films. Unlike a single-component polymer film, the structure of the equilibrated film is not always a priori known. Even if known, it may be difficult to generate an equilibrated starting configuration for the MD simulation. One way to produce polymer films computationally is to follow the experimental procedure of dissolving the polymer in a solvent and then evaporating the solvent. By controlling the evaporation rate, one can in principle obtain structures, which as in experiment may be in equilibrium or not depending on the rate of evaporation. Within such an approach we, with computer simulations, investigated the importance of relative stiffness between the segments A and B for the morphology of the thin film. In this work we study evaporation of solvent from a solution of both diblock and multiblock copolymers. The blocks of the copolymers are mutually repulsive, so in the dry state they are locally phase separated. The substrate has no preference for either of the two blocks. We find that changes in relative stiffness of the block changes the morphology of the film. By increasing the stiffness we can control the resulting structure from lamellar to one which exhibits a microscopic phase separation into small isolated domains. The

10.1021/ma048509s CCC: $27.50
Published on Web 10/27/2004

stability of these phases is investigated by simulating systems with random block lengths.

The paper is organized as follows: In section 2 we discuss the method used including a description of the force field, the system setup and size, as well as how solvation and evaporation is modeled. Benchmark calculations on diblock polymers are also reported in section 2. Section 3 is devoted to an account of the simulation results, with emphasis on how differences in stiffness in the coblock polymer segments affect the morphology, evaporation rate, surface roughness, and domain size. A discussion of our findings and short summary are presented in section 4.

2. Model and Simulation Details

1. Model. Molecular dynamics is a powerful tool for studying large and complex systems and is therefore extensively used in modern science. Depending on the scope of the problem there are a number of methods available: Atomistic simulations employing quantum mechanical methods are used when knowledge of chemical properties is necessary. Parametrized force fields are used when the detailed chemical bonding is not as crucial although the atomistic character is. A united atom approach, where groups of atoms are the dynamic quantity, for example, a CH_2 group, is often used to study longer times and larger systems since the number of degrees of freedom and the range of time scales in the problem are both significantly reduced. The reduction in degrees of freedom can be taken a step further to the so-called the coarse-grained bead−spring model, where the polymers are represented by beads and connected by flexible springs. The bead−spring model has proven very useful for studying long-time phenomena in polymers.[36,37] In this study, we use the coarse-grained bead−spring model since the large scale and long-time morphology of thin polymer films are the main issues.

The bead−spring model employed in the simulations has been described extensively elsewhere.[38,39] The copolymers consist of two different species but of the same mass m, and the solvent is modeled as single monomers of mass m. The interaction potential between the different nonbonded pairs of monomers is the standard 6−12 Lennard−Jones potential

$$U_{\mathrm{LJ}}(r) = \begin{cases} 4\epsilon_{\alpha\beta}\left\{\left(\frac{\sigma_{\alpha\beta}}{r}\right)^{12} - \left(\frac{\sigma_{\alpha\beta}}{r}\right)^{6}\right\} + \epsilon_{\mathrm{LJ}}, & r \le r_c \\ 0, & r > r_c \end{cases} \quad (1)$$

where r is the distance between monomers and ϵ_{LJ} is a constant added so that the potential is continuous at $r = r_c$. Here we take $\sigma_{\alpha\beta} = \sigma$ for all α, β and $r_c = 2.5\sigma$ except between the two different species of the copolymer where the interaction is purely repulsive, with $r_c = 2^{1/6}\sigma$. $\epsilon_{\alpha\beta}$ (see below) and σ define the units of energy and length, respectively. Bonded monomers also interact with an additional anharmonic potential known as the FENE potential.[38,39]

The bonded and nonbonded interactions constitute a bead−spring model describing fully flexible polymer chains interacting with a solvent. An important property of polymers exhibiting nanoscale phase separation—crucial to fuel-cell applications—is the presence of a stiff backbone. The model above was therefore amended with a cosine bending potential between three neighboring beads along the same chain[40]

$$U_{\mathrm{bend}}(\theta) = k_{\theta,\alpha}(1 - \cos\theta) \quad (2)$$

where $k_{\theta,\alpha}$ is the elasticity parameter for the α type of the angle potential which depends on the type of species of the central monomer and $\cos\theta_i = (\hat{\mathbf{r}}_i - \hat{\mathbf{r}}_{i-1})\cdot(\hat{\mathbf{r}}_{i+1} - \hat{\mathbf{r}}_i)$, where $(\hat{\mathbf{r}}_i - \hat{\mathbf{r}}_{i-1})$ is the unit vector in the bond direction. The persistence length of the chains in a melt as a function of stiffness $k_{\theta,\alpha}$ is given in ref 36.

With this framework we are able to study polymers with different stiffness along the chain, different polymer−polymer interactions, as well as different solvation properties. We denote the solvent monomers as type 1 and the two species of the polymer as type 2 and 3, which corresponds to the softer (segment A) and stiffer (segment B) part of the polymer chain, respectively. We explored a range of solvent−polymer interactions: $\epsilon_{13} = \epsilon$, 0.8ϵ, and 0.6ϵ, while $\epsilon_{12} = \epsilon$ always. For $\epsilon_{13} = 0.6\epsilon$, the solvent and polymer phase separated on a macroscopic scale and $\epsilon_{13} = 0.8\epsilon$ behaved similar to the neutral solvent case $\epsilon_{13} = \epsilon$ regarding the final morphology. In this paper we report results for $\epsilon_{\alpha\beta} = \epsilon$.

Our main focus is on how polymer stiffness affects the morphology; we, in particular, studied the cases of A−B segments with corresponding stiffness parameters $\{k_{\theta,\alpha A}/\epsilon, k_{\theta,\alpha B}/\epsilon\} \equiv \{k_{\alpha A}, k_{\alpha B}\}$ being {1,1} (flexible−flexible), {1,3} (flexible−stiff), {1,10} (flexible−very stiff), and {3,10} (stiff−very stiff). For a homopolymer melt at density $\rho\sigma^3 = 0.85$, the persistence length for $k_\alpha = 1$ and 3 is $l_p/\sigma = 2.2$ and 5.6, respectively, while for $k_\alpha \gtrsim 6$, the system forms a nematic phase.[40]

2. Simulation Details. For all the systems studied the initial cell is created by randomly building the polymer chains between two flat walls. To place all of the beads into the simulation box at a desired density $\rho = 0.8\sigma^{-3}$, the beads are allowed to overlap. The overlap is then removed by applying a soft, nonbonded potential until the actual potential could be switched on. The system is then equilibrated at pressure $P \simeq 0$ and temperature $T = \epsilon/k_B$ by allowing the distance between the two walls to adjust. The monomer−surface interaction potential is given by the 9−3 LJ potential with a cutoff distance of $r_c^w = 2.2\sigma$.[41] The equations of motion were integrated with a velocity−verlet algorithm with a time step of $\Delta t = 0.01\tau$, where $\tau = m(\sigma/\epsilon)^{1/2}$. The simulations were performed at constant temperature T using the Langevin thermostat with damping constant $\gamma = 0.5/\tau$. After equilibration, the top wall is then removed so that the solution is in contact with a vacuum. Periodic boundary conditions are used in the x and y directions, and the solvent evaporates in the positive z direction.

Modeling of the nonequilibrium process of evaporation is done by using the massively parallel grand canonical MD code LADERA[42] which is a hybrid of the massively parallel MD code LAMMPS[43] and a grand canonical Monte Carlo (GCMD) code.[44] Briefly, GCMD periodically performs Monte Carlo molecular insertion and deletion attempts in a control volume located at the very right side of Figure 1. The probability of insertion and deletion in the control volume is determined by the chemical potential desired in this region. In our simulation the chemical potential for this region is chosen so that all the solvent monomers entering this volume are removed from the system, i.e., the system is in contact with a vacuum. Evaporation was continued until at least 94% of the solvent was evaporated. Beyond this point the rate of evaporation is so slow that it is no longer practical to continue the simulation. To remove the remaining solvent monomers from the system within a reasonable amount of time, the control volume was expanded to the entire system. The remaining solvent monomers were removed over the course from 2500τ to 5000τ time steps. The resulting polymer melt was then allowed to thermalize for at least 5000τ time steps, a short time in comparison with the evaporation stage which took more than $10^5\tau$.

We mainly studied multiblock copolymers of two different system sizes: a "small" system with 100 000 particles and initial geometry $40\sigma \times 40\sigma \times 80\sigma$ and a "large" system with 400 000 particles and initial geometry $80\sigma \times 80\sigma \times 80\sigma$ or $40\sigma \times 40\sigma \times 320\sigma$. The number of particles was equally distributed between solvent and polymer. Thus, the "small" systems contain 500 chains, each 100 segments long with alternating A and B segments of 10 beads each. The large systems are comprised of 2000 chains by construction four times the surface area of the small system; hence, one run on the large system is equivalent to four runs of the small system. Computationally, it is too demanding to mimic the polydispersion measured in fabricated films due to the very large experimental spread in chain lengths. Initial steps toward describing polydispersity were taken by allowing random segment lengths: the length

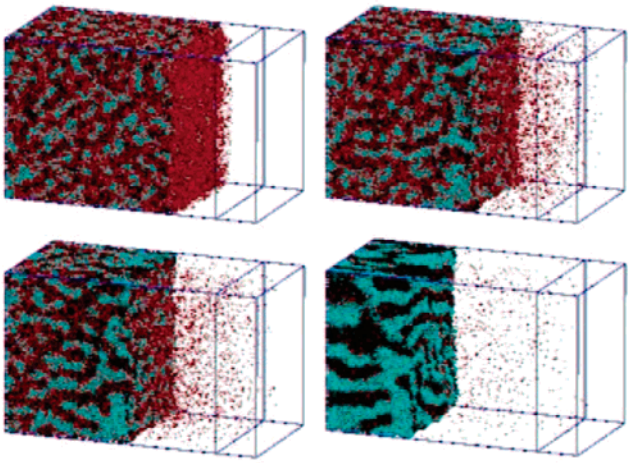

Figure 1. Four perspective views of the evaporation process at 0%, 25%, 50%, and 92% evaporated solvent for multiblock copolymer with stiffness $k_{\alpha A} = k_{\alpha B} = 1$. Solvent monomers are colored red, and type 2 and type 3 polymer monomers are colored green and black, respectively. Note that the long-range order appears during evaporation; the initial solvated system is disordered. Subsequent figures in the article are 2D cuts and slices either perpendicular to the direction of evaporation or along the direction of evaporation (side view). The direction of evaporation is $\hat{z}$,and the two perpendicular directions are $\hat{x}$ and $\hat{y}$.

of each segment was taken randomly from a uniform distribution between 8 and 12. The model system has a polydispersity index of 1.02, measured as the ratio of number- and weight-average degrees of polymerizations of the blocks of 10.2 and 10.0, respectively. The polydispersity is in practice very close to monodispersion and not to be compared to experimental systems. Some differences can be identified already at this level of polydispersion though, and we discuss these findings, without claim of making predictions for experimental ranges of polydispersion. Unless specified, the results presented are for the "large" systems.

We first investigated the effectiveness of our model by studying symmetric diblock copolymers consisting of 2500 chains of total length of 20 beads with stiffness $\{k_{\alpha A}, k_{\alpha B}\} = \{1, 1\}$ and $\{1,10\}$. We simulated three different cases: diblock copolymer solutions where one-half of the system is solvent and stiffness $\{1,1\}$ and $\{1,10\}$, and pure diblock copolymer melt of stiffness $\{1,1\}$ between two flat surfaces. As expected, the lowest energy state is a lamellar phase, see Figure 2; the two different blocks phase separate completely. In the pure melt case a grain boundary appears in the middle of the film; the top and bottom halves have different orientation. The grain boundary was not removed during the simulation time ($8.5 \times 10^4\tau$). Evaporation of solvent removes this problem, as we can see in the figure a global lamellar phase is recovered due to evaporation of solvent. The evaporation process took $8.0 \times 10^4\tau$. For stiffness $\{1,10\}$ case, however, a grain boundary remains near the middle of the film after evaporating all the solvent in the system. The lamellar close to the substrate is slightly rotated from the surface lamellar structure, resulting in frustration near the middle of the film. Note that since the surfaces have no preference for either of the two blocks, the lamellar structure in all cases, as expected,[4,14,22,23] is perpendicular to the surfaces.

The multiblock system is more complex, and although the chains have random orientation in solution, the equilibrium structure of the pure melt is not readily known. A lamellar structure has low energy but requires a high degree of order, decreasing the entropy. The analysis of section 3.2 suggests that a lamellar structure is the most stable.

3. Results

1. Evaporation Dynamics. Figure 3a shows the total polymer density profile, while Figure 3b shows the

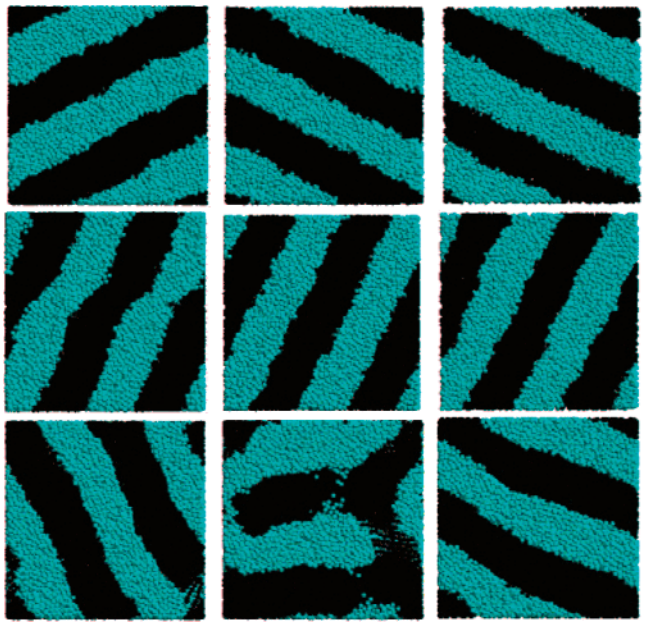

Figure 2. (Top) Top view of pure diblock copolymer melt without solvent and between two flat surfaces at three heights from the substrate: 6σ, 24σ, and 32σ. (Middle and bottom) Top view of a diblock melt of stiffness $\{1,1\}$ and $\{1,10\}$, respectively, after evaporation of a solvent, initially 50% of the system, at heights 6σ, 20σ, and 30σ and 2σ, 12σ, and 24σ, respectively.

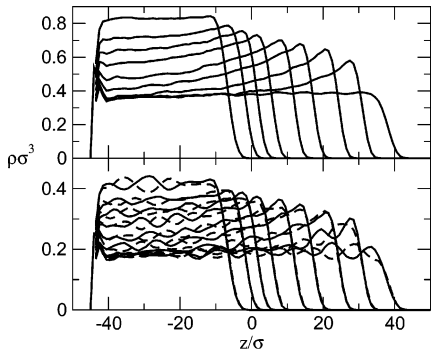

Figure 3. Time evolution of the (a) total density profile and (b) flexible (solid line) and stiff (broken line) segments of the polymer as a function of time for multiblock copolymer with $k_{\alpha A} = 1$, $k_{\alpha B} = 10$. The profiles are at different times and from right to left correspond to $t/(10^3\tau) = 0$, 4, 10, 20, 30, 45, 60, 80, and 233.

density profile of flexible and stiff parts of the polymer chain as a function of time for the multiblock copolymer with $\{k_{\alpha A}, k_{\alpha B}\} = \{1,10\}$. The total density profile displays similar behavior, as recently observed for evaporation of solvent from fully flexible homopolymers.[45] There is a polymer density gradient at the film/vapor interface, and its magnitude decreases as the density of the polymer increases to its melt density value ($\rho \simeq 0.8\sigma^{-3}$). Both parts of the polymer (flexible and stiff) show a density gradient at the film/vapor interface. In addition, they show a gradient structure in the system as can be seen from the oscillation of the individual densities. The gradient structure is formed due to the difference in surface tension between the two polymer segments. The more flexible part of the segment has lower surface tension and is thus mainly exposed to the vapor interface. The other cases, $\{1,3\}$ and $\{3,10\}$, display similar behavior, while the $\{1,1\}$ case shows the same density gradient but no gradient

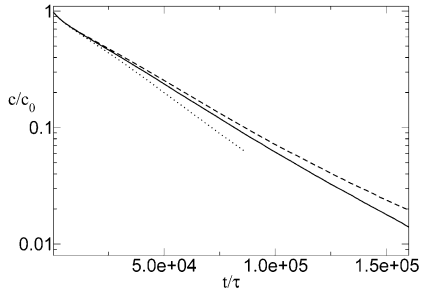

Figure 4. Logarithmic plot of the concentration of solvent remaining in the film divided by its initial concentration c_0 for $\{k_{\alpha A}, k_{\alpha B}\}=\{1,1\}$ (dot line), {1,10} (solid line), and {3,10} (broken line).

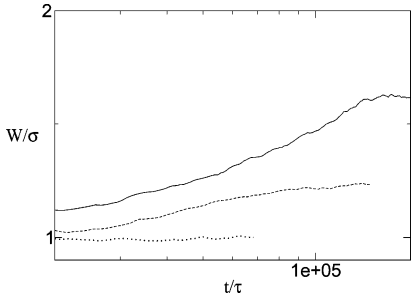

Figure 5. Interface width versus time for $\{k_{\alpha A}, k_{\alpha B}\}=\{1,1\}$ (dotted line), {1,10} (solid line), and {3,10} (dashed line).

in the structure since the surface tension for both segments is the same (graph not shown).

The magnitude of the polymer density gradient at the film/vapor interface affects the rate of solvent evaporation from the system. Figure 4 shows the concentration of solvent monomers c remaining in the film normalized by the initial solvent concentration c_0. It takes almost the same amount of time to evaporate the first 94% of the solvent and the next 4% of solvent. All three cases show the same exponential solvent evaporation behavior, but the rate of evaporation decreases slightly as the stiffness of the polymer segments increases.

The dependence of the width of the polymer/vapor interface on the stiffness of the polymer segments can be found from

$$W^2(L, t) = \frac{1}{L^2}\sum_i [h_i(t) - \overline{h(t)}]^2 \qquad (3)$$

where L^2 for our case is the number of grids on the surface ($L = 20$), $h_i(t)$ is the height of the surface at grid i and time t, and $\overline{h(t)}$ is the average height at time t. Figure 5 shows a plot of the interface width as a function of time. The width of the interface is constant for the {1,1} case but increases with time for the {3,10} and {1,10} cases. The simulations were run longer for the {3,10} and {1,10} cases until a steady-state value is reached. The interface width depends on the relative stiffness of the polymer segments.

2. Final Morphologies. The resulting morphologies after evaporation for successively stiffer segments are shown in Figure 6. Evaporation is a nonequilibrium process, and the paths taken can differ between different simulation runs. The morphologies shown are found in a number of simulations. All parameter sets were at least run for one "small" and one "large" system, the latter equivalent to four runs for the small cell since similar morphology is found in the four quadrants.

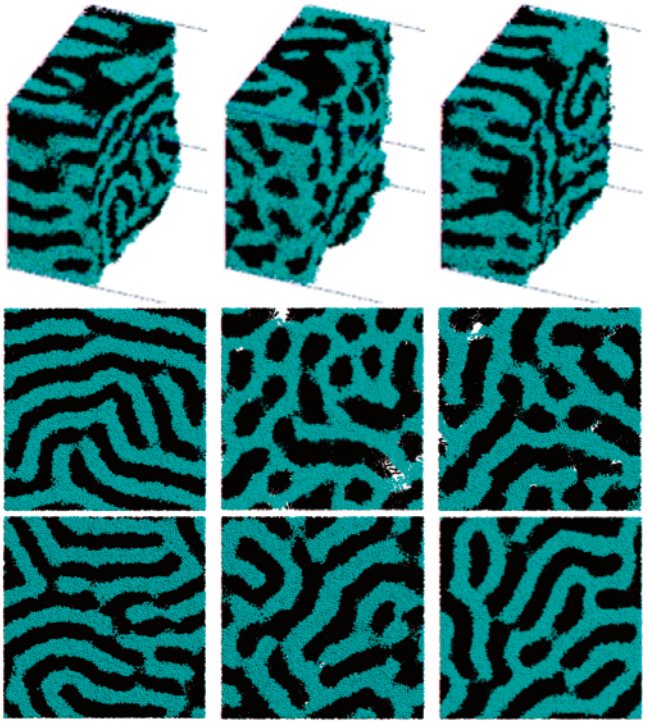

Figure 6. Final morphologies for six cases of varying stiffness and polydispersity. (Top) 3D perspective view of stiffnesses {1,1}, {1,10}, and {3,10}, respectively, and the simulation box is partly shown. The 2D morphologies are slices at height 30σ from the substrate that is close to the free surface, which is about 36σ from the substrate. (Middle, from left) {1,1}, {1,10}, {3,10}. (Bottom, from left) {1,1} polydispersed, {1,10} polydispersed, and {1,3}.

There is a significant change in morphology with increased stiffness. In more detail, the {1,1} case exhibits a lamellar structure with long parallel domains perpendicular to the substrate. Perfect ordering with parallel domains is not reached, although that is not to be expected given the complexity of the multiblock polymers. Little change in the morphology is observed in the time scale of our simulation, and thus the configurations are in local, though not necessarily in global, equilibrium. Though the systems are liquid like, the morphologies can be frozen in by reducing the temperature.

The {1,3} case is largely lamellar; however, the domains are less parallel, shorter, and small domains begin to form. {1,3} is clearly a transition case, it exhibits partial properties from the flexible−flexible and flexible−stiff systems. A case with stiff−very stiff segments {3,10} is also shown in Figure 6; it is characterized by a lamellar main structure, although the parallel domains are wider and shorter than in the {1,1} case.

The flexible−very stiff case {1,10} displays a significantly different morphology: the flexible component constitutes a matrix for isolated domains of the stiff component. Surprisingly, the stiff component (dark) does not percolate the plane; the stiff domains are completely surrounded by the flexible component. This is in stark contrast to the other cases in Figure 6 which are bicontinuous. These cylindrical features are not isolated occurrences but have been observed in both small and large systems with large stiffness differences. The small systems with neutral solvent and stiffness {1,15} and {3,15} (not shown) resulted in a similar morphology. The large system with high aspect cell ratio $40\sigma \times 40\sigma$

Table 1. Average End−End Distance $l = \sqrt{(r_i - r_{i+9})^2}$ of Each Segment[a]

$\{k_{\alpha A}, k_{\alpha B}\}$	$\langle l_A \rangle$ (σ)	$\langle l_B \rangle$ (σ)
{1,1}	4.01	4.04
{1,3}	3.96	5.42
{1,10}	3.93	7.84
{3,10}	4.76	7.86

[a] For flexible segments the length is, as expected, smaller than for stiff ones. For the stiffness 10 cases, the distances approach the maximum limit, $l_{max} = 9$.

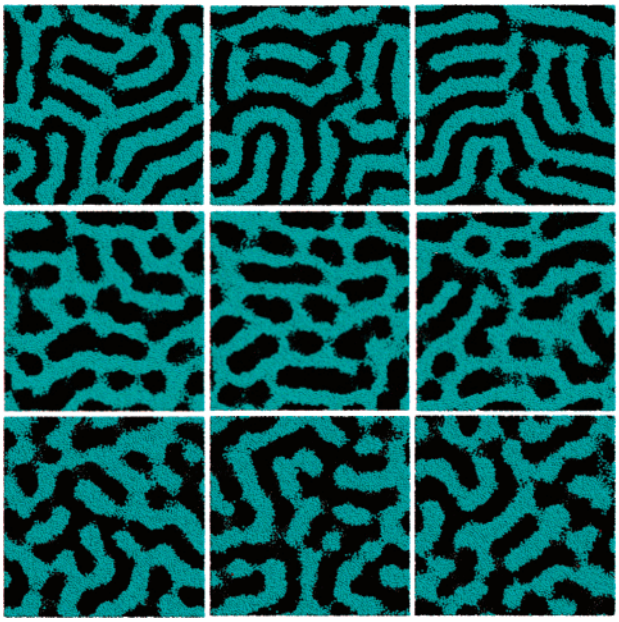

Figure 7. Three rows from the top are for stiffnesses {1,1}, {1,10}, and {1,10} polydispersed, respectively, at three heights from the substrate 15σ, 20σ, and 25σ. The cylindrical domains are formed at the free surface and in the bulk; the substrate is not necessary for formation. Several circular features are sustained through more than three layers, which is longer than the segment length. The differences in morphology are persistent through the sample, see Figure 9.

$\times$ 320σ and stiffness {1,10} also showed the nonpercolating morphology. The difference in stiffness appears to drive the transition since the {3,10} system exhibits a mainly lamellar structure.

Table 1 gives the average end to end lengths of each block for the main cases. As expected, stiff blocks are more extended and therefore effectively longer than flexible ones; however, when paired with a stiffer segment, the average length is reduced, which can be seen by comparing {1,1}, {1,3}, and {1,10} as well as {1,3} with {3,10}. Although approaching the maximum end−end distance in cases {1,10} and {3,10}, there is some curvature; the stiff segments are not rods.

Next, we focus on the cylindrical features in the {1,10} case and investigate the morphology in more detail, comparing it to the {1,1} and {1,10} polydispersed systems. The dominating pattern persists through the film, as illustrated in Figure 7. Note that the substrate is by design nondiscriminant between A and B segments. In the {1,10} case cylinders are formed at the surface. How these patterns propagate through the film is shown in Figure 7, which also shows how the polydispersity reduces ordering. Forming domains at the surface was confirmed by simulations in the high-aspect ratio cell.

In Figure 8 we show perpendicular slices of the $\{k_{\alpha A}, k_{\alpha B}\}$={1,10} system. The structure persists through

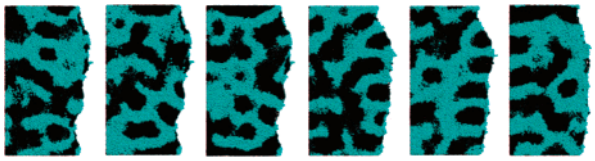

Figure 8. Vertical morphology cuts for {1,10} yz plane at $x = 25\sigma$, 30σ, and 35σ followed by xz plane at $y = 25\sigma$, 30σ, and 35σ. Together with Figures 7 and 9 they suggest cylindrical features, although not directed perfectly perpendicular to the surface.

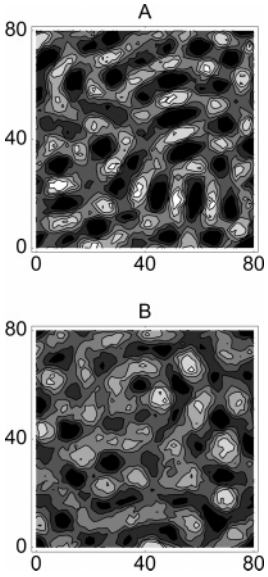

Figure 9. Density, $\tilde{\rho}_3$, of stiff component in the {1,1} (A) and {1,10} (B) cases, integrated over all z. Dark regions are for low density, while light regions are for high density.

the sample. The domains shown in Figure 6 for the {1,10} case are not lamellar; they are more like cylinders, extending more than one segment length from the surface.

A third view of the {1,10} and {1,1} systems is presented in Figure 9, showing the density, $\tilde{\rho}_3$, of the stiff component (type 3) integrated over z: $\tilde{\rho}_3(x, y) = \int \rho_3(x, y, z)\, dz$. The lamellar character of the flexible−flexible case is evident even after the averaging through the film since the lamellars are perpendicular to the substrate, as noted earlier in the section. In contrast, the {1,10} system exhibits circular symmetry; dense regions are surrounded by low-density regions. Note that there are regions comprised of solely stiff segments, percolating the film from substrate to surface. The substrate−surface distance is 40σ, implying that segments from multiple chains are combined. Figures 6−9 are all consistent with mainly cylindrical features of the stiff component dominating the morphology.

Of interest is the stability of the resulting films: can they be interconverted after evaporation by simply changing the bending stiffness and then annealing it for a reasonable time? When investigating this aspect we discovered asymmetry in changes in morphology of postevaporation. We compared the two main cases, {1,1} and {1,10}, by interchanging their stiffnesses after evaporation and subsequently annealing the systems. The final, mainly lamellar phase of {1,1} is largely unaffected by interchanging stiffness to {1,10} and annealing for 53 000τ. However, the final, isolated domain phase of {1,10} behaves differently; it is rapidly destroyed when the stiffness is changed to {1,1} and

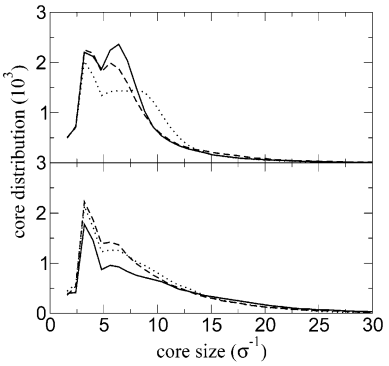

Figure 10. Core distribution plot showing the distribution of 1D length of the phases parallel to the surface (top) and perpendicular to the surface (bottom). In both figures the solid line is for stiffness {1,1} and type 2 monomers and the dashed line and dotted line are for stiffness {1,10} and type 2 and type 3 monomers, respectively. For the {1,1} case, type 3 has the same solid curve within the error of the simulation.

annealed for 5000τ; a lamellar phase is formed. This behavior is in line with the finding that even small polydispersion can perturb the microdomain separated phase discussed earlier.

3. Core Size Distribution. The one-dimensional (1D) distribution of domain lengths, known as the core distribution, is shown in Figure 10 for stiffness {1,1} and {1,10}. The distribution is calculated by partitioning the system volume into small cubes ($0.8\sigma \times 0.8\sigma \times 0.8\sigma$), basically one bead per cube, and counting in 1D ($\hat{x}$, $\hat{y}$, or $\hat{z}$ direction) type i monomers that are adjacent to each other, i.e., no other type of monomer in between. This defines the core size. The distribution is thus the number of occurrences of the core sizes over many lines either parallel or perpendicular to the surface. Cores in the direction parallel to the surface are taken along either the $\hat{x}$ or $\hat{y}$ direction.

The core distribution gives information about the domain sizes, in particular in isotropic systems. However, it may not fully describe a lamellar phase with lamellar orientation at an angle with the $\hat{x}$, $\hat{y}$, and $\hat{z}$ directions. The smallest significant structure in the distribution is the lamellar spacing; it is followed by a broader distribution stemming from lines at an angle with the lamellar domains and, when applicable, additional features. The distribution for type 2 and type 3 for the {1,1} case are the same. When comparing the two main cases, {1,1} and {1,10}, we make three observations. First, in the distribution parallel to the substrate, the {1,1} structure shows two peaks, corresponding to one and two average segment lengths from Table 1. Type 2 of {1,10} also shows similar behavior. Second, also in the parallel direction, the stiff part of the {1,10} case (type 3) shows a wide bell-shaped distribution around the average end−end distance of ∼7; it is consistent with the cylindrical features, depending on the specific cut through the cylinder the core distribution varies around a mean value. Third, the perpendicular distribution is, compared to the parallel one, shifted toward longer domains for both the {1,1} and {1,10} cases. This shift is caused by the orientation of both lamellar and cylindrical features being oriented perpendicular to the substrate. The {1,1} case exhibits slightly stretched segments; however, the distributions for long lengths are very similar.

4. Angular Orientation. The differences in lamellar spacings appearing in Figures 6 and 10 have two causes.

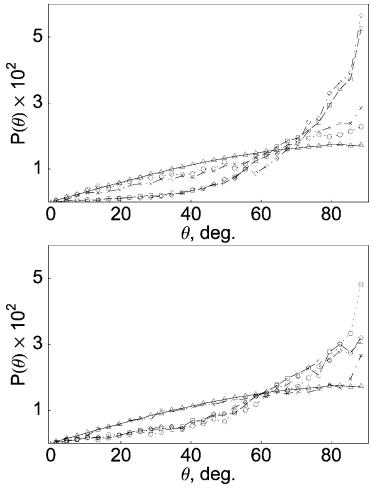

Figure 11. (Top) Distribution of angle between the z axis and the vector between the first and last bead of the stiff segment (type 3). 90° is perpendicular to the evaporation direction. Symbols are as follows: {1,1} (circle/dotted); {1,3} (×/dashed); {1,10} (square/dashed); {3,10} (diamond/dot−dashed); (random distribution) (triangles/solid). Both cases with stiff segments exhibit a large degree of orientation. (Bottom) Angular distribution for the {1,10} case for 18σ thick slices taken at three different heights from the substrate: at the substrate (circles/dotted), midway between surface and substrate (i.e., 10σ above the substrate) (square/dashed), at the surface (i.e., 18σ above the substrate) (diamond/dot−dashed). Also shown are random distribution (triangles/full) and in solvent before evaporation (×/dot−dashed).

First, the stiffer segments are more extended (see Table 1); second, stiff segments are more ordered, as evident from Figure 11. The figure shows the probability distribution of angles with the normal plane for the segment end−end vectors. When compared to a random distribution, also shown in the figure, we find that the stiff case deviates significantly from a random distribution. The main distribution is around 90°; the segments are thus oriented parallel to the surface and the substrate, perpendicular to the direction of evaporation. The second panel shows the distribution at different distances from the substrate; with the exception of the 90° ordering imposed by the substrate in the lowest slice, the distributions are similar. The lamellar packing thus persists through the sample, beyond the extent of individual segments, and is not suppressed at the surface. For comparison, the distribution of the segments in the equilibrated solution is also shown in the figure and as expected has the form of a random distribution.

4. Summary and Discussion

We have shown that it is possible to computationally produce model polymer films by dissolving the polymer in a solvent and subsequently evaporating the solvent. This method is applicable when, as in most cases, the structure of the film is not a priori known. It is also a method to produce, as in experiments, structures that are only in local equilibrium. For diblock copolymer films formed in this way, a global lamellar phase was found in approximately the same time it took to equilibrate a pure melt. For multiblock copolymers, we showed how this method, as in experiment, can be used to produce films that are in local, not necessarily in global, equilibrium. For fully flexible multiblock copolymers mainly lamellar phase is formed, but an ordered microphase- separated phase is formed when stiff seg-

ments are combined with flexible ones. The cylinder-like phase, which is probably a nonequilibrium state, is not straightforward to form. Initially, in solvent, the system is disordered, for example, the distribution of vertical angle for the end to end vectors is very close to a random distribution, see Figure 11. After evaporation, on the other hand, the angular correlation is dominant and the percolating cylinders are comprised of stiff segments from multiple polymer chains, excluding the flexible component into a surrounding matrix. Selective etching of the flexible surrounding matrix has potential to result in a periodic pattern on the nanoscale. The resulting system is highly anisotropic; the stiff component percolates the system in the direction perpendicular to the surface; however, it does not percolate in the plane parallel to the surface, as is evident from Figure 6. Properties depending on the morphology, for example, proton conduction and interdiffusion of small molecules, are likely to show similar anisotropy. However, the degree of anisotropy is very sensitive to, for example, weak, polydispersion. Additionally, as discussed in section 3.1, we observe that evaporation slows down with increased stiffness of the blocks while the surface roughness depends on the difference in stiffness between the blocks.

It is difficult to quantitatively compare our multiblock simulation results with experiment since there have been few experiments on the morphology of multiblock ($n > 3$) copolymers. Spontak and Smith[46] examined the morphologies of symmetric poly(styrene-*b*-isoprene)$_n$ multiblock copolymers (for $n \leq 4$) cast into a Teflon mold followed by solvent evaporation and found a lamellar morphology to all symmetric copolymers investigated, similar to our flexible−flexible multiblock case. They also found a decrease in lamellar spacing with increasing in n, which was also confirmed by self-consistent mean-field theory.[47] We observe a similar trend in our simulation: the lamellar spacing for the diblock system is about 10σ, while for the multiblock system it is about 7σ. The cylinder-like morphology we observed for a symmetric stiff−flexible linear multiblock copolymer is open for future experimental test.

The present study shows that even highly nonequilibrium processes, like thin-film casting by evaporation, not only can be simulated in a single "proof of principle" simulation but it is feasible to explore trends. Here we focused on the effects of stiffness on morphology; future direction of this work includes investigating how side branches affect the morphology, temperature cycling during evaporation, as well as interdiffusion of selective solvent into the various morphologies and effect of rate of evaporation. The resulting morphologies can be utilized as templates for atomistic simulations to explore pathways for ionic conduction in atomistic studies.

Acknowledgment. Sandia is a multiprogram laboratory operated by Sandia Corporation, a Lockheed Martin Company, for the United States Department of Energy's National Nuclear Security Administration under contract DE-AC04-94AL85000.

References and Notes

(1) Mansky, P.; Harrison, C. K.; Chaikin, P. M. *Appl. Phys. Lett.* **1996**, *68*, 2586.
(2) Park, M.; Harrison, C.; Chaikin, P. M.; Register, R. A.; Adamson, D. H. *Science* **1997**, *276*, 1401.
(3) Hashimoto, T.; Tsutsumi, K.; Funaki, Y. *Langmuir* **1997**, *13*, 6869.
(4) Huang, E.; Russell, T. P.; Harrison, C.; Chaikin, P. M.; Reigster, R. A.; Hawker, C. J.; Mays, J. *Macromolecules* **1998**, *31*, 1, 7641.
(5) Rosa, C. D.; Park, C.; Thomas, E. L.; Lotz, B. *Nature* **2000**, *405*, 433.
(6) Li, R. R.; Dapkus, P. D.; Thompson, M. E.; Jeong, W. G.; Harrison, C.; Chaikin, P. M.; Register, R. A.; Adamson, D. H. *Appl. Phys. Lett.* **2000**, *76*, 1689.
(7) Peters, R. D.; Yang, X. M.; Wang, Q.; de Pablo, J. J.; Nealey, P. F. *J. Vac. Sci. Technol. B* **2000**, *18*, 3530.
(8) Green, P. F.; Limary, R. *Adv. Colloid Interface Sci.* **2001**, *94*, 53.
(9) Black, C. T.; Guarini, K. W.; Milkove, K. R.; Baker, S. M.; Russel, T. P.; Tuomi- nen, M. T. *Appl. Phys. Lett.* **2001**, *79*, 409.
(10) Krausch, G.; Magerle, R. *Adv. Mater.* **2002**, *14*, 1579.
(11) Bates, F. S.; Fredrickson, G. H. *Ann. Rev. Phys. Chem.* **1990**, *41*, 525.
(12) Krausch, G. *Mater. Sci. Eng. Rep.* **1995**, *14*, *1*.
(13) Lambooy, P.; Russell, T. P.; Kellogg, G. J.; Mayes, A. M.; Gallagher, P. D.; Satija, S. K. *Phys. Rev. Lett.* **1994**, *72*, 2899.
(14) Wang, Q.; Yan, Q.; Nealey, P. F.; de Pablo, J. J. *J. Chem. Phys.* **2000**, *112*, 450.
(15) Huinink, H. P.; van Dijk, M. A.; Brokken-Zijp, J. C. M.; Sevink, G. J. A. *Macromolecules* **2001**, *34*, 5325.
(16) Fasolka, M. J.; Mayes, A. M. *Annu. Rev. Mater. Res.* **2001**, *31*, 323.
(17) Segalman, R. A.; Schaefer, K. E.; Fredrickson, G. H.; Kramer, E. J. *Macromolecules* **2003**, *36*, 4498.
(18) Wang, Q.; Nealey, P. F.; de Pablo, J. J. *Macromolecules* **2001**, *34*, 3458.
(19) Segalman, R. A.; Hexemer, A.; Kramer, E. J. *Macromolecules* **2003**, *36*, 6831.
(20) Knoll, A.; Horvat, A.; Lyakhova, K. S.; Krausch, G.; Sevink, G.; Zvelindovsky, A. V.; Magerle, R. *Phys. Rev. Lett.* **2002**, *89*, 035501.
(21) Koneripalli, N.; Singh, N.; Levicky, R.; Bates, F.; Gallagher, P. D.; Satija, S. K. *Macromolecules* **1995**, *28*, 2897.
(22) Kellogg, G. J.; Walton, D. G.; Mayes, A. M.; Lamggoy, P.; Russell, T. P.; Gallagher, P. D.; Satija, S. K. *Phys. Rev. Lett.* **1996**, *76*, 2503.
(23) Mansky, P.; Russell, T. P.; Hawker, C. J.; Pitsikalis, M.; Mays, J. *Macromolecules* **1997**, *30*, 0, 6810.
(24) Fasolka, M. M.; Banerjee, P.; Mayes, A. M. *Macromolecules* **2000**, *33*, 5702.
(25) Pickett, G. T.; Balazs, A. C. *Macromol. Theory Simul.* **1998**, *7*, 249.
(26) Sommer, J.; Hoffmann, A.; Blumen, A. *J. Chem. Phys.* **1999**, *111*, 3728.
(27) Morkved, T. L.; Lu, M.; Urbas, A. M.; Ehrichs, E. E.; Jaeger, H. M.; Mansky, P.; Russell, T. P. *Science* **1996**, *273*, 932.
(28) Mansky, P.; DeRouchey, J.; Russell, T. P.; Mays, J.; Pitsikalis, M.; Morkved, T.; Jaeger, H. *Macromolecules* **1998**, *31*, 4399.
(29) Walton, D. G.; Kellogg, G. J.; Mayes, A. M.; Lambooy, P.; Russell, T. P. *Macromolecules* **1994**, *27*, 6225.
(30) Mansky, P.; Chaikin, P.; Thomas, E. *J. Mater. Sci.* **1985**, *30*, 1987.
(31) Sivaniah, E.; Hayashi, Y.; Iino, M.; Hashimoto, T. *Macromolecules* **2003**, *36*, 5894.
(32) Rollet, A.-L.; Diat, O.; Gebel, G. *J. Phys. Chem. B* **2002**, *106*, 3033.
(33) Kreuer, K. D. *J. Membr. Sci.* **2001**, *185*, 29.
(34) Reiter, G.; de Gennes, P. *Eur. Phys. J. E* **2001**, *6*, 25.
(35) Niu, S.; Saraf, R. F. *Macromolecules* **2003**, *36*, 2428.
(36) In *Monte Carlo and Molecular Dynamics Simulations in Polymer Science*; Binder, K., Ed.; Oxford: New York, 1995.
(37) Kremer, K.; Grest, G. In *Monte Carlo and Molecular Dynamics Simulations in Polymer Science;* Binder, K., Ed.; Oxford: New York, 1995; Chapter 4, pp 194−271.
(38) Grest, G. S.; Kremer, K. *Phys. Rev. A* **1986**, *33*, 3628.
(39) Kremer, K.; Grest, G. S. *J. Chem. Phys.* **1990**, *92*, 5057.
(40) Auhl, R.; Everaers, R.; Grest, G. S.; Kremer, K.; Plimpton, S. J. *J. Chem. Phys.* **2003**, *119*, 12718.
(41) Sides, S. W.; Grest, G. S.; Stevens, M. J. *Macromolecules* **2002**, *35*, 566.
(42) Thompson, A. P.; Heffelfinger, G. S. *J. Chem. Phys.* **1999**, *110*, 10693.
(43) Plimpton, S. J. *J. Comput. Phys.* **1995**, *117*, *1*.
(44) Heffelfinger, G. S.; van Swol, F. *J. Chem. Phys.* **1994**, *100*, 7548.
(45) Tsige, M.; Grest, G. S. *Macromolecules* **2004**, *37*, 4333.
(46) Spontak, R. J.; Smith, S. D. *J. Polym. Sci.* **2001**, *39*, 947.
(47) Rasmussen, K.; Kober, E. M.; Lookman, T.; Saxena, A. *J. Polym. Sci., Part B* **2003**, *41*, 104.

MA048509S